

1 **How well does an Earth System Model represent the occlusion of extratropical**
2 **cyclones?**

3

4 Catherine M Naud,^a Gregory S Elsaesser,^a Poushali Ghosh,^b Jonathan E Martin,^b Derek J Posselt^c
5 and James F. Booth^d

6 ^a *Applied Physics and Applied Mathematics, Columbia University/NASA GISS, New York, NY*

7 ^b *Atmospheric and Oceanic Sciences, University of Wisconsin-Madison, Madison, WI*

8 ^c *Jet Propulsion Laboratory, California Institute of Technology, Pasadena, CA*

9 ^d *Department of Earth and Atmospheric Sciences, City College of New York, NY*

10

11 *Corresponding author: Catherine Naud, cn2140@columbia.edu*

12

ABSTRACT

13

14 Extratropical cyclones are the main providers of midlatitude precipitation, but how they will
15 change in a warming climate is unclear. The latest NASA Goddard Institute for Space Studies
16 (GISS) Earth System models (ESMs) accurately simulate the location and structure of cyclones,
17 though deficiencies in the depiction of cloud and precipitation are found. To provide a new
18 process-level context for evaluation of simulated cloud and precipitation in the mid-latitudes,
19 occluded cyclones are examined. Such cyclones are characterized by the formation of a thermal
20 ridge, maintained via latent heat release in the wider three-dimensional trough of warm air
21 aloft (TROWAL) in the occluded sector. Using a novel method for objective identification of
22 occluded cyclones, the simulation of occlusions in the latest GISS-E3 model is examined. The
23 model produces occluded cyclones, adequately depicting the thermal and kinematic structure
24 of the thermal ridge, with realistic depth and poleward tilt. Nevertheless, E3 occlusions are less
25 frequent than observed and systematically shifted poleward and towards the exit region of the
26 climatological storm tracks. Compared to CloudSat-CALIPSO cloud retrievals across the thermal
27 ridge, the dependence of cloud properties on thermal ridge strength is well represented,
28 though at the expense of producing low ice mass clouds too often at high altitudes (i.e. “too
29 many, too tenuous”). Overall, E3 produces significantly more precipitation in occluded versus
30 non-occluded cyclones, demonstrating the importance of accurately representing occlusions
31 and associated hydrological processes in ESMs.

32 **1. Introduction**

33 The majority of the precipitation in the mid-latitudes (30°-60°N/S) is delivered by
34 extratropical cyclones and their attendant fronts, up to 80% in the winter (Hawcroft et al., 2012;
35 Catto et al., 2012). These systems are also responsible for the most extreme of precipitation
36 events (Pfahl and Wernli, 2012; Kunkel et al., 2012). As the Earth’s climate changes, concurrent
37 changes in extratropical cyclones, their attendant precipitation distributions, as well as
38 associated extremes are the subject of active research (e.g. Bengtsson et al., 2009; Pfahl and
39 Wernli, 2012; Kunkel et al., 2013; Marciano et al. 2015). Future climate predictions suggest an
40 increase in the precipitation associated with extratropical cyclones (Zhang and Colle, 2018),

41 forced by changes in temperature and moisture availability (Yettella and Kay, 2017), not so much
42 by changes in cyclone strength (Sinclair and Catto, 2023). In addition, many studies have shown
43 the importance of latent heat release in areas of cloud and precipitation formation for cyclone
44 development (Binder et al., 2016), but cloud and precipitation representation, and their
45 associated latent heating, in Earth System Models (ESMs) are still deficient (e.g. Catto et al.,
46 2015; Naud et al., 2020). Therefore, the ESM representation of moist processes associated with
47 extratropical cyclones needs to be further evaluated to increase confidence in future climate
48 predictions.

49 One aspect of the cyclone life cycle that is strongly influenced by latent heat release is the
50 occlusion process, whereby cyclones adopt a characteristic thermal structure as they reach their
51 post-mature phase. First introduced by Bergeron (Jewell, 1981), the warm occlusion process
52 involves the cold front encroaching upon, and eventually ascending, the warm frontal surface
53 (due to static stability contrasts, Stoelinga et al., 2002). This promotes the production of a
54 wedge of warm air aloft displaced poleward of the warm front. This warm wedge manifests as a
55 thermal ridge between the cyclone center and the peak of the warm sector (Martin, 1998a,b,
56 1999a,b; Schultz and Vaughan, 2011 and references therein). Warm moist air is forced to ascend
57 cyclonically from the warm sector boundary layer through the thermal ridge, predominantly via
58 positive vorticity advection by the thermal wind (Sutcliffe, 1947; Martin 1999a,b), filling a
59 sloping three-dimensional region called the Trough of Warm air Aloft or TROWAL (Crocker et al.,
60 1947; Penner, 1955) with clouds and precipitation. It is in association with this feature, not the
61 surface occluded front, that some of the heaviest precipitation observed in the occluded
62 cyclone often occurs (Martin, 1998b; Grim et al, 2007; Han et al. 2007; Naud et al., 2024).
63 Therefore, the occluded thermal ridge (OTR) is the location of substantial latent heat release
64 which, in turn, substantially shapes the tropopause-level potential vorticity (PV) and
65 tropospheric thermal structure of the canonical warm occlusion (Posselt and Martin, 2004).
66 Thus, examination of the structure and evolution of occluded cyclones in an ESM indirectly
67 contributes to evaluation of the model's fidelity in representing latent heat release and its
68 impacts. Focusing on occlusions, synoptic entities with an identifiable structure and a well
69 understood synergistic relationship to cloud and precipitation production, affords a real test of

70 the fidelity of the model's representations of the component physical processes it hopes to
71 replicate as well as their interactions.

72 To the authors' knowledge there have been no prior studies that document the occurrence,
73 the structure or the evolution of occluded cyclones in ESMs. This is partly because, until
74 recently, there was no automated method to identify occlusions in models. In Naud et al.
75 (2023), such a method was designed and applied to the Modern Era Retrospective analysis for
76 Research and Applications version 2 (MERRA-2; Gelaro et al., 2017). The same method can be
77 applied to any gridded dataset, observational or otherwise, thus making it suitable for
78 application to ESMs, enabling novel process-level model evaluation. In this study, we apply the
79 identification methodology to the Goddard Institute for Space Studies (GISS) latest Earth system
80 model (GISS-E3). Using MERRA-2 and combined observations from CloudSat (Stephens et al.
81 2002) and CALIPSO (Winker et al. 2007) for reference, we evaluate E3's ability to represent
82 occlusions, their structure, and their cloud properties in the OTR. This analysis is aimed at
83 addressing the following questions: 1) Does an ESM represent the occlusion process?, and 2)
84 How well does it represent the thermal, kinematic and cloud structure of the occluded cyclone?
85 Additionally, we seek to demonstrate that examination of an evolving synoptic entity, like an
86 occluded cyclone, which inherently depends on the interaction of scales ranging from the
87 continental to the microphysical, can assist in identifying potential model deficiencies.

88 The examination of these issues is organized as follows. Section 2 presents details
89 concerning the model and its integration, the datasets used for comparison, as well as the
90 various tools needed for the intended analysis. The evaluation of the model's depiction of
91 occlusions is detailed in section 3 and progresses from examination of the large-scale
92 environment within which the storms form to the cyclone scale and then finally to the thermal
93 ridge scale. Section 4 includes a discussion on why and how an accurate representation of
94 occlusions in E3 informs understanding of the model's depiction of precipitation distribution as
95 well as extremes. A summary and conclusions are available in section 5.

96 **2. Model, datasets and methodology**

97 This section describes the model to be tested, the various algorithms and tools employed
98 throughout the analysis and the datasets used for comparison.

99 *a. The CMIP6 NASA Goddard Institute for Space Studies Earth System Model E3*

100 GISS-E3, the latest and most advanced of three GISS contributions to CMIP6 (E2.1, E2.2 and
101 E3), is the focus of this study. Compared to the other two GISS models, E3 comprises
102 substantial upgrades to multiple physics parameterizations, an increase in vertical resolution
103 (from 40 to 110 layers), and use of a machine learning algorithm to more objectively calibrate or
104 “tune” the ESM (Elsaesser et al., 2024). An early summary of the physics upgrades relative to
105 E2.1 is available in Cesana et al. (2019), and of the particular tuned candidate known as “Tun2”
106 analyzed here in Cesana et al.(2021) and Li et al. (2023). A selection of the pertinent physics
107 schemes that directly affect cloud and precipitation are summarized below:

- 108 - Planetary Boundary Layer physics: includes novel heat flux equations without use of a
109 critical Richardson number (Cheng et al. 2020), along with the moist turbulence scheme
110 based on Bretherton and Park (2009).
- 111 - Convection: the upgraded double plume model described in Kelley et al. (2020) for E2.1
112 was further modified to include cold pool representation (Del Genio et al. 2015) and
113 improved ice microphysics (Elsaesser et al. 2017a).
- 114 - Large-scale cloud parameterization: a prognostic stratiform precipitation (MG2
115 microphysics; Gettelman and Morrison 2015) and a new stratiform cloud fraction
116 scheme (Smith 1990) were implemented.

117 In GISS-E3, ice water path (IWP) and liquid water path (LWP) are substantially decreased
118 from previous versions of the model, and in closer agreement with observational estimates
119 (Elsaesser et al. 2017a, b). Substantial improvements in simulating convective phenomena are
120 also noted (e.g., tropical cyclones; Russotto et al. 2022).

121 The current analysis utilizes an atmosphere-only free-running integration of E3, forced with
122 prescribed transient, monthly varying sea surface temperatures. Our focus is on the 2006 –
123 2011 period. We use the 2.5°x2° horizontal resolution configuration as in Cesana et al. (2019;
124 2021), and Li et al. (2023), although c90 (~1°) resolution will be the final resolution submitted
125 to CMIP6. The 3-hourly model output includes: two-dimensional sea-level pressure and surface
126 precipitation, and profiles (on 110 vertical levels from 979 to 0.0035 hPa) of temperature,
127 specific humidity, geopotential height, wind, vertical velocity, cloud fraction, ice and liquid water

128 content for both suspended and falling condensate. Because GISS-E2.1 is also part of the CMIP6
129 model ensemble, we performed a cursory evaluation of the occlusion depiction in this model
130 (same horizontal resolution, but lower vertical resolution and substantially different cloud
131 parameterizations; full details in Kelley et al., 2020) and summarized the results in the
132 supplemental material document.

133 *b. Tracking extratropical cyclones*

134 To identify the location of extratropical cyclones and track their evolution in time, we use
135 the algorithm of Bauer and Del Genio (2006). This algorithm, fully described and evaluated in
136 Bauer et al. (2016), utilizes gridded sea level pressure fields and searches for local minima. To
137 briefly summarize, the algorithm first imposes thresholds for the central pressure and the
138 difference in pressure relative to the surrounding area to decide whether the identified minima
139 are indeed depressions. Upon identification, the candidate centers are tracked in time, with a
140 number of thresholds imposed for the rate of change in central pressure and its maximum
141 horizontal displacement (no more than 720 km in 6 hours). At the end, a list of cyclone tracks
142 lasting at least 36 hours is generated, with information on the latitude and longitude of each
143 center every 6 hours from cyclone initiation to dissipation. This algorithm was applied and
144 tested by Bauer et al. (2016) on the ERA-Interim reanalysis (Dee et al., 2011). The same tracking
145 algorithm is applied to E3 sea level pressure fields, with cyclone information stored every 6
146 hours for consistency.

147 *c. Identification of occlusions*

148 Using the cyclone track history obtained with the Bauer and Del Genio method, an occlusion
149 identification algorithm, as described in Naud et al. (2023), is then applied. The algorithm
150 searches for 6-hourly cyclone instances along each track with an occluded thermal ridge: a two-
151 dimensional projection of the full three-dimensional TROWAL region. Using the 1000-500 hPa
152 thickness (ϕ') field, the thermal ridge is identified around each cyclone center (within $\pm 20^\circ$
153 latitude, from 10° west to 20° east) by assessing the divergence of the unit vector of the ϕ'
154 gradient ($\hat{n} = \frac{\nabla\phi'}{|\nabla\phi'|}$). Grid cells around the cyclone are flagged if 1) they indicate convergence
155 (using $F = (\nabla \cdot \hat{n})|\nabla\phi'| < -1 \times 10^{-6} \text{ m}^{-1}$) and 2) they are not in regions of heterogenous topography

156 (standard deviation of surface altitude amongst nearest neighbors less than 300m). Using the
157 cyclone tracks, this cluster of flagged grid cells is tracked in time using a cyclone-centered grid if
158 at a minimum it encompasses 4 grid cells at the $2.5^{\circ} \times 2^{\circ}$ resolution of the model. If these
159 converging regions spatially overlap in time in this reference grid for at least two consecutive 6-
160 hour time steps, and the period over which the overlap occurs contains or follows the time of
161 maximum cyclone intensity (i.e. minimum in sea level pressure at the center over the entire
162 lifetime), the cyclone track and the individual 6-hourly instances are identified as being
163 occluded. This algorithm when applied to Model E3 takes into account its $2.5^{\circ} \times 2^{\circ}$ spatial
164 resolution (c.f. Naud et al., 2023).

165 *d. Reanalyses and CloudSat-CALIPSO for Reference Datasets*

166 The analysis presented below conducts a step by step evaluation of E3 and utilizes different
167 reference datasets along the way. To evaluate E3 cyclone locations, we use the ERA-interim
168 database first created by Bauer et al. (2016), called the MAP Climatology of Midlatitude
169 Storminess (MCMS). A new version of the cyclone track database is being developed using the
170 same algorithm applied to the more recent ERA5 reanalysis (Hersbach et al., 2020) but this
171 database was not ready at the time of this work. Because cyclones tend to occur on the polar
172 side of the upper level jets, for consistency, ERA-interim 250 hPa zonal winds are also used.
173 These are the only tests that make use of ERA-Interim, any other test that requires information
174 typically provided with a reanalysis makes use of Modern Era Retrospective Analysis for
175 Research and Applications version 2 (MERRA-2; Gelaro et al., 2017) instead. This choice was
176 motivated by its relative novelty compared to ERA-interim and its relatively higher spatial
177 resolution.

178 Using the MCMS cyclone tracks, we obtained MERRA-2 thickness fields for each 6-hourly
179 cyclone instance and applied the algorithm described in the previous section to these.
180 Therefore, we will refer to this subset of cyclones identified as occluded as the MERRA-2
181 database of occluded cyclones. This publicly-available database of occluded cyclones was
182 produced for the period 2006-2017 and provides the list of cyclone instances that are occluded
183 as well as the location of the thermal ridge. A full description of this database is provided in
184 Naud et al. (2023), the only difference here is that the MERRA-2 thickness fields were coarsened

185 to a $2.5^{\circ} \times 2^{\circ}$ resolution first, to match E3 spatial resolution. This modified MERRA-2 occluded
186 cyclone collection serves as our observational compositing reference. Additionally, all the
187 analyses that explore the environmental characteristics of E3 occluded cyclones use for
188 comparison MERRA-2 6-hourly profiles of geopotential height, temperature, wind, specific
189 humidity and vertical velocity, available at $0.625^{\circ} \times 0.5^{\circ}$ horizontal resolution on 42 levels from
190 1000 to 0.1 hPa.

191 To characterize cloud properties, we appeal to remotely sensed observations: specifically
192 employing the CloudSat-CALIPSO GEOPROF-LIDAR (Mace et al., 2008; Mace and Zhang, 2014)
193 and 2C-ICE (Deng et al. 2010) products as the sources for observed cloud hydrometeor states in
194 cyclones. The GEOPROF-LIDAR product combines hydrometeor identifications from both the
195 radar and lidar and provides the location of up to five cloud layer base and top heights in the
196 CloudSat footprint ($\sim 1.3 \text{ km} \times 1.7 \text{ km}$). However, because CloudSat cannot distinguish falling
197 from suspended particles, these cloud layers are more appropriately termed “hydrometeor
198 layers”. We use the altitude information on cloud layer bases and tops to create a vertical profile
199 of hydrometeor presence, which indicates whether cloud and/or precipitation are present at
200 250 m resolution in the vertical.

201 The 2C-ICE product provides ice water content profiles obtained using both lidar 532 nm
202 attenuated backscatter and radar reflectivity profiles ingested into an optimal estimation
203 algorithm. These profiles are provided at the resolution of the CloudSat horizontal footprint (1.4
204 km across \times 1.7 km along track). The uncertainty in retrieved IWC is estimated to be less than
205 30% (Deng et al., 2013), although that estimate might be substantially larger in precipitating
206 clouds and with increasing convective core vertical depth (i.e., in the tropics). The reported IWC
207 has a minimum threshold that is dictated by limits in both lidar and radar detectability.
208 However, the model does not have such limitations and will provide very small values of IWC
209 that are currently unobservable. To ensure a fairer comparison, we define a minimum IWC for
210 use in E3 evaluation that best matches the retrieval capability. For this, we constructed a
211 temperature dependent threshold on IWC based on a 10-granule collection of 2C-ICE retrievals,
212 informed by data analysis provided by Deng (personal communication). The threshold (IWC_{\min})
213 is computed as follows:

214 $IWC_{\min}=10^{-3.26474}$ where $T \leq 210K$

215 $IWC_{\min}= 10^{((T-276.543)/20.3823)}$ where $T > 210 K$

216 where T is the temperature of each model grid cell level. The E3 IWC is set to zero in any grid
217 cell level where $IWC(T) < IWC_{\min}$. Tests reveal a notable difference in mean IWC without
218 incorporation of thresholding, with E3 estimates closer to observations upon application of the
219 threshold.

220 *e. Compositing Methodology*

221 To facilitate comparison between E3 and MERRA-2 occluded cyclones, we developed a
222 compositing methodology that enables use of sparse datasets and provides useful insight on
223 occlusion characteristics (Naud et al., 2023; 2024). Two types of geometric reference frames are
224 used: one is a plan view that considers the cyclone as a whole and uses the cyclone center as an
225 anchor for averaging various fields while the other focuses on vertical transects across the
226 thermal ridge.

227 For the cyclone-centered composites, the gridded fields are first projected onto a rectangular
228 grid with meridional and zonal directions expressed in distance from the cyclone center,
229 centered on the point of minimum in sea-level pressure, with maximum dimensions ± 4000 km
230 west-east and ± 3000 km south-north. The re-gridded fields from each cyclone are then
231 superimposed before calculating the mean of all cyclones. Note that we do not apply any
232 rotation on the cyclone fields to take account of the direction of propagation.

233 For the vertical transect composites, the thermal ridge serves as the anchor. The algorithm
234 described in Section 2c identifies the thermal ridge in each occluded cyclone as a set of
235 contiguous points at which $F = (\nabla \cdot \hat{n})|\nabla\phi'|$ is smaller than a threshold value ($-1 \times 10^{-6} \text{ m}^{-1}$). A
236 regression line (in latitude/longitude) is then calculated through this cluster. This line
237 represents the orientation of the thermal ridge axis. At the median longitude of this thermal
238 ridge axis a transect line is drawn perpendicular to it. Finally, the thermal ridge axis line is slid
239 along the transect line until it reaches the coincident 700 hPa θ_e maximum (hereafter referred
240 to as $\max(\theta_e)$). The location of this maximum is the anchor for the composites (see Naud et al.,
241 2023 for additional details). As in Naud et al. (2023), we use $\max(\theta_e)$ throughout as a metric to
242 categorize the thermal ridges (from “cold” to “warm”).

243 For MERRA-2 and the GISS models, geopotential heights, θ_e and vertical velocity profiles -
244 and, for E3 only, cloud fraction and IWC profiles - are aggregated along the perpendicular line
245 using a nearest neighbor approach and arranged into distance bins of 200 km width from 1500
246 km on the equator-west side of the ridge to 1500 km on its polar-east side. Using the location of
247 $\max(\theta_e)$ at 700 hPa as the zero point, the perpendicular transects of all the thermal ridges are
248 superimposed and their average calculated.

249 For the composite transects that involve use of the CloudSat-CALIPSO retrievals, the method
250 has to be altered since the orbits provide data in random locations around the thermal ridges. A
251 full description of the approach adopted is available in Naud et al. (2024, see their Figure 2). In
252 this case, all observational profiles (i.e., hydrometeor masks, ice water mass) in a broader region
253 are used, as long as they are located between the two perpendiculars at the ridge extremities
254 within ± 1500 km of any point along the ridge. In this case, the closest point along the ridge to
255 each observed profile is used as the anchor to obtain the distance information needed to
256 populate the transects. The effect of this random sampling of the entire ridge area as opposed
257 to a simple perpendicular at the median longitude along the ridge was tested in Naud et al.
258 (2024), and good agreement was found when this was applied to MERRA-2 θ_e profiles (c.f. their
259 Figure 3).

260 **3. Evaluation of occlusions in model E3**

261 For the analysis of occlusions in E3, we first focus on the Northern Hemisphere (NH) winter
262 season (December, January and February) for the 5-year period of 2006-2011. This hemisphere
263 and season have been the foci of active research on occlusions, so there is ample literature
264 providing additional references. Our prior experience suggests that 5 years is of sufficient
265 duration to furnish a large, representative sample size without incurring an undue burden in
266 terms of data storage.

267 *a. Are there occluded cyclones in E3?*

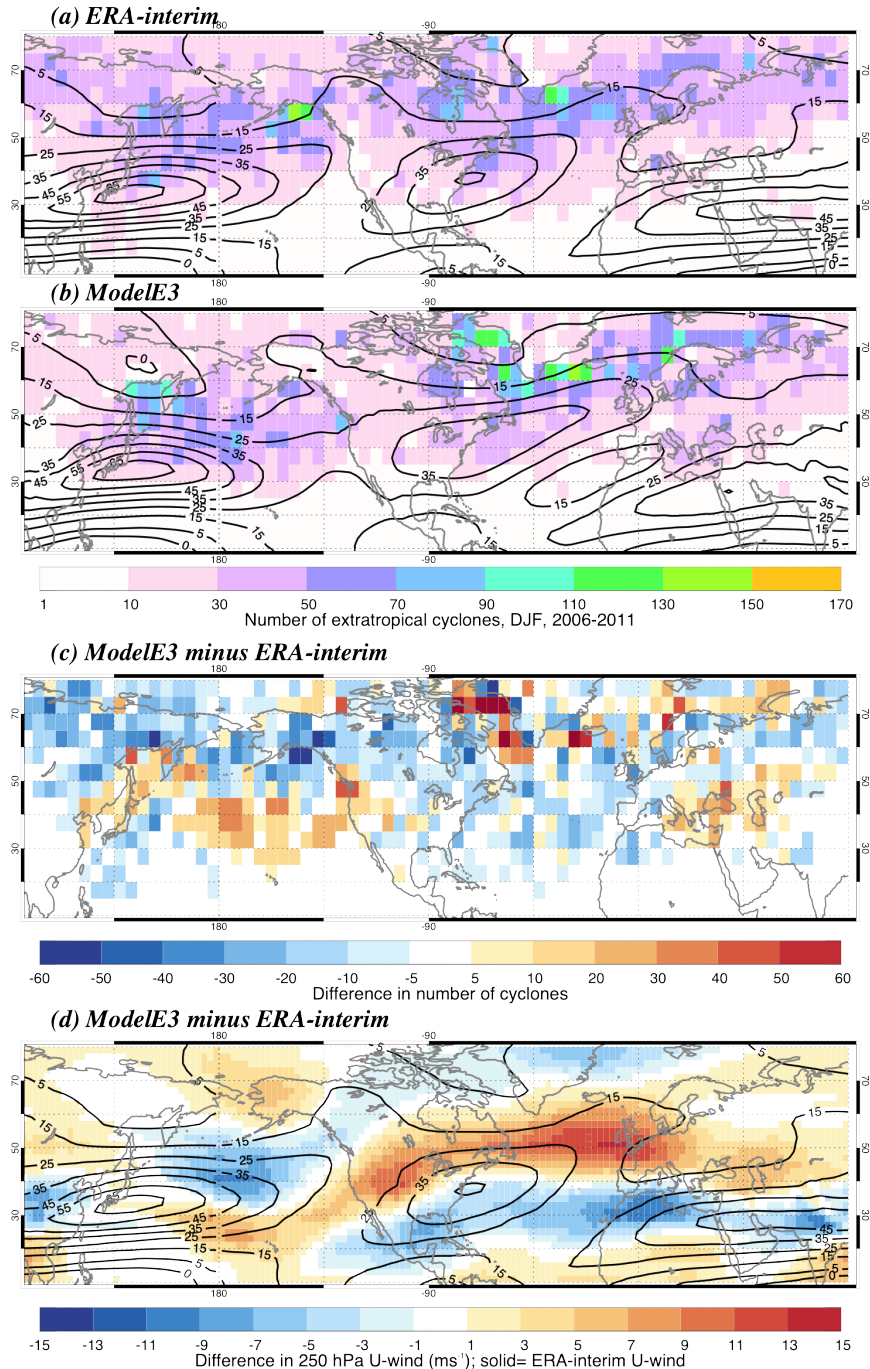
268 As discussed in Section 2.a, the Model E3 integration is performed using prescribed sea
269 surface temperatures (free-running, with no nudging). Therefore, the cyclones that emerge in
270 the model are not expected to match, in time and space, those that occurred in the real world.

271 However, since the simulated climate presumably resembles the actual climate, extratropical
272 cyclones are expected to collectively occur in places and at times that are comparable to
273 reanalysis datasets. The first step, as a result, is to examine how closely the storm track and
274 climate of E3 match those obtained with ERA-Interim for the same period of time. This first
275 comparison includes all cyclones identified and tracked over both land and ocean.

276 Cyclones tend to congregate in regions referred to as the storm tracks (e.g. Hoskins and
277 Hodges, 2002, for the NH), which are typically found between Japan and Alaska in the north
278 Pacific basin and between the US Carolina coastline and Norway in the Atlantic ocean. The ERA-
279 Interim reanalysis indicates two hot spots for the 2006-2011 winters (Figure 1a): one off the
280 east coast of southern Greenland and another along the Alaskan south coast. These were also
281 reported in Hoskins and Hodges (2002) and Neu et al. (2013). The Mediterranean storm track is
282 relatively weak, possibly because the tracker uses sea level pressures which, according to
283 Hoskins and Hodges (2002), tend to miss small systems, such as those typically found in this
284 region, that are more effectively identified using measures such as 850 hPa vorticity.

285 Model E3 represents the location of the NH winter storm tracks realistically (Figure 1b) but
286 with some notable differences. The total number of cyclones is close to that observed for the
287 entire hemisphere, but E3 1) tends to have more cyclones occurring near the exit of the Atlantic
288 storm track than the reanalysis, 2) does not produce sufficient cyclones along the coast of
289 Alaska and the Pacific storm track exit region generally and 3) produces too many along the
290 entire southern coast of Greenland. Overall, the preferred storm locations in the model's
291 Atlantic basin tend to be found poleward of those in the reanalysis and equatorward in the
292 Pacific basin (Fig.1c). These shifts are consistent with the differences in the upper- level jet,
293 expressed as the mean zonal wind at 250 hPa in Figure 1d.

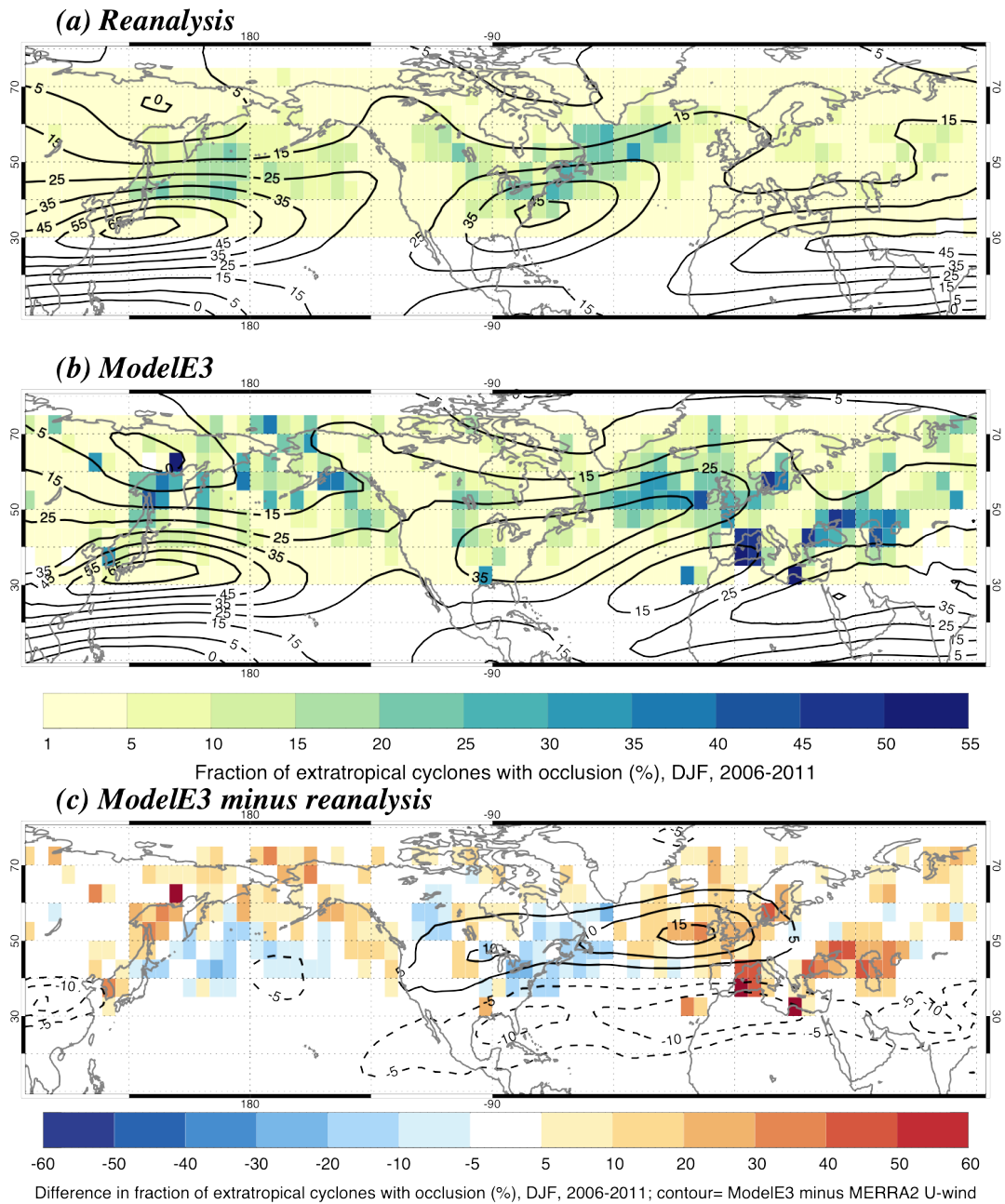
294



295

296 Figure 1: Number of extratropical cyclone centers in 5°x5° regions (color, from 1 to 160 in
 297 increments of 10), that occurred in December, January and February 2006-2011 in (a) ERA-
 298 Interim and (b) ModelE3, with black contours showing the corresponding zonal wind speed at
 299 250 hPa (from 5 to 65 m/s, every 10 m/s); (c) the difference in number of cyclones between
 300 ModelE3 and ERA-interim (color, from -60 to 60, in increments of 10); and (d) the difference in
 301 250hPa zonal wind between Model E3 and ERA-Interim for the same period (color, from -15 to
 302 15 m/s every 2 m/s). The black solid contour in (d) show the 250 hPa ERA-Interim zonal wind,
 303 in 10 m/s increments from 5 to 65 m/s.

304
305 With these climatological differences in mind, we next examine the location of the occluded
306 cyclones. Here we consider all cyclone instances that are flagged as occluded, including those
307 that belong to the same track. Then we consider the fraction of all cyclone instances in a $5^{\circ} \times 5^{\circ}$
308 region that are identified as occluded over both land and ocean (c.f. Supplemental material Fig.
309 S1 for the actual numbers). For reference, in each box we calculate the ratio of occluded
310 cyclones, as identified with MERRA-2 thickness fields, to the total number of cyclones in the
311 MCMS database. In this reference dataset, the fraction of occluded cyclones tends to be
312 relatively larger in the entrance and middle regions of the storm track in both ocean basins
313 (Figure 2a) consistent with the fact that occlusions develop preferentially in the left exit
314 quadrant of the upper level jets. As a result, there are relatively larger fractions to the west of
315 the dateline than to the east in the Pacific and west of Iceland rather than east of it in the
316 Atlantic. However, the fraction of occluded cyclones in E3 exhibits some clear discrepancies with
317 respect to reanalysis, in both ocean basins (Figure 2b). In the Pacific, the occlusions are more
318 evenly distributed and noticeably more frequent along the Alaskan coast in E3 than in the
319 reanalysis. In the Atlantic ocean, they tend to occur more frequently towards the exit region of
320 the storm track than they do in the reanalysis. Cyclones also occlude in the Mediterranean Sea
321 45% more often in Model E3 than in the reanalysis, though the physical basis for this notable
322 discrepancy is unknown. Figures 2a and 2b also show the corresponding 250 hPa zonal winds
323 averaged for all time steps when an occluded cyclone was identified. In Figure 2a, we now use
324 MERRA-2 winds for consistency with the occlusion identification (differences between MERRA-2
325 and ERA-interim zonal winds are much smaller than between either reanalysis and E3, see
326 supplemental material, Fig. S2). While differences in jet location and in fraction of occluded
327 cyclones appear to be collocated in the Atlantic basin (Fig. 2c), this is not the case in the Pacific
328 basin or Mediterranean region. Therefore, differences in the large-scale circulation climatology
329 alone do not explain differences in where occlusions are favored in E3.
330



331

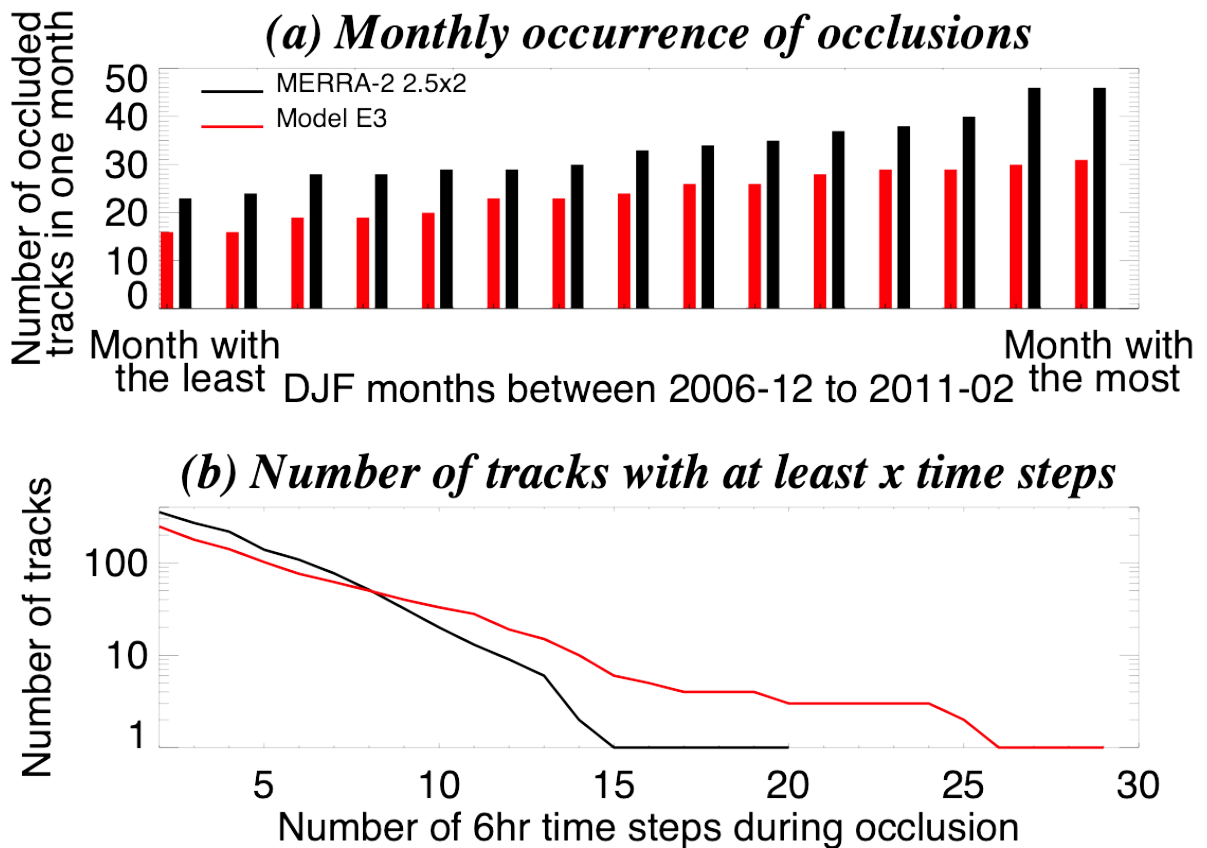
332 Figure 2: Fraction of all cyclones per 5°x5° cell that are identified as being occluded in (a)
 333 the reanalysis and (b) ModelE3 (%), in color, from 1 to 55% in 5% increments). The solid
 334 contours indicate the zonal 250hPa wind averaged for times when an occluded cyclone occurs (in
 335 m/s, from 5 to 65 m/s in 10 m/s increments). (c) shows the corresponding difference between
 336 ModelE3 and MERRA-2. Solid (dashed) contours show the difference in 250 hPa zonal wind
 337 between Model E3 and MERRA-2 collected at the time of occlusion from 5 to 15 m/s (from -15
 338 to -5 m/s) in 5m/s increments.

339

340 Examining the occluded portion of the cyclone lifecycles more specifically, we find there are
 341 fewer cyclones undergoing occlusion in E3 than in reanalysis (Figure 3a). Figure 3a also reveals a

342 larger variability in the number of occluded cyclones per month in MERRA-2 than E3. However,
 343 for those cyclones that do occlude, they retain an occluded structure for a longer period of time
 344 in E3 (many for well over three days; Figure 3b). It is clear that Model E3 simulates occluded
 345 cyclones, but disparities with reanalysis in their preferred location, frequencies and duration call
 346 for an exploration of the structure of the occluded cyclones in E3. Are the mechanisms involved
 347 in the occlusion process realistically represented?

348



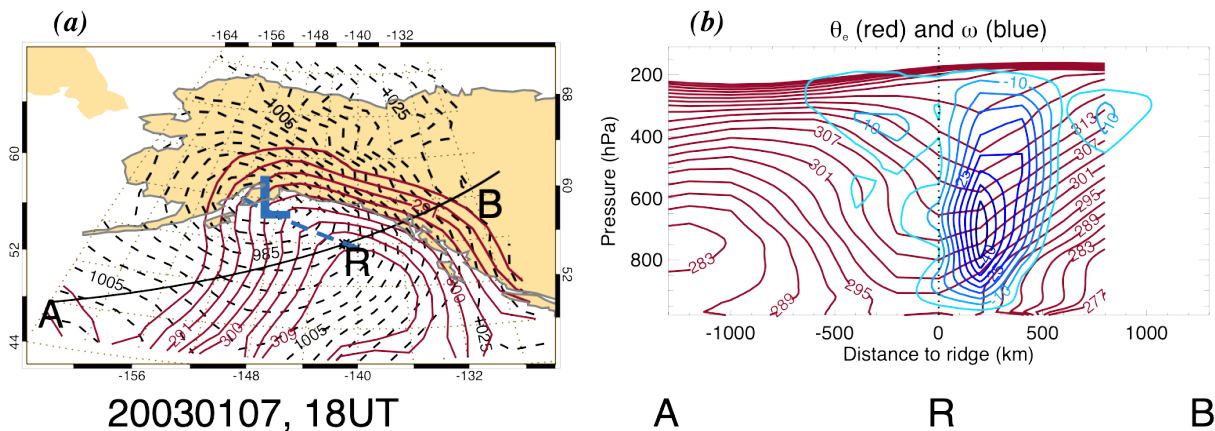
349

350 Figure 3: (a) Number of tracks that are at some point occluded, per month arranged from
 351 least to most populated for MERRA-2 (black; 500 tracks in total), and Model E3 (red; 359
 352 tracks in total) and (b) the total number of tracks with a minimum number of 6-hourly time steps
 353 from 2 to 30 in MERRA2 (black) and Model E3 (red solid).

354 *b. Is the structure of the occluded cyclones in E3 realistic?*

355 An example of an occluded cyclone in E3 is first examined. Figure 4 provides the 700 hPa θ_e
 356 distribution around the cyclone center and across the occluded thermal ridge (OTR). As is typical
 357 of occluded cyclones, the θ_e field indicates an area to the east of the cyclone center with

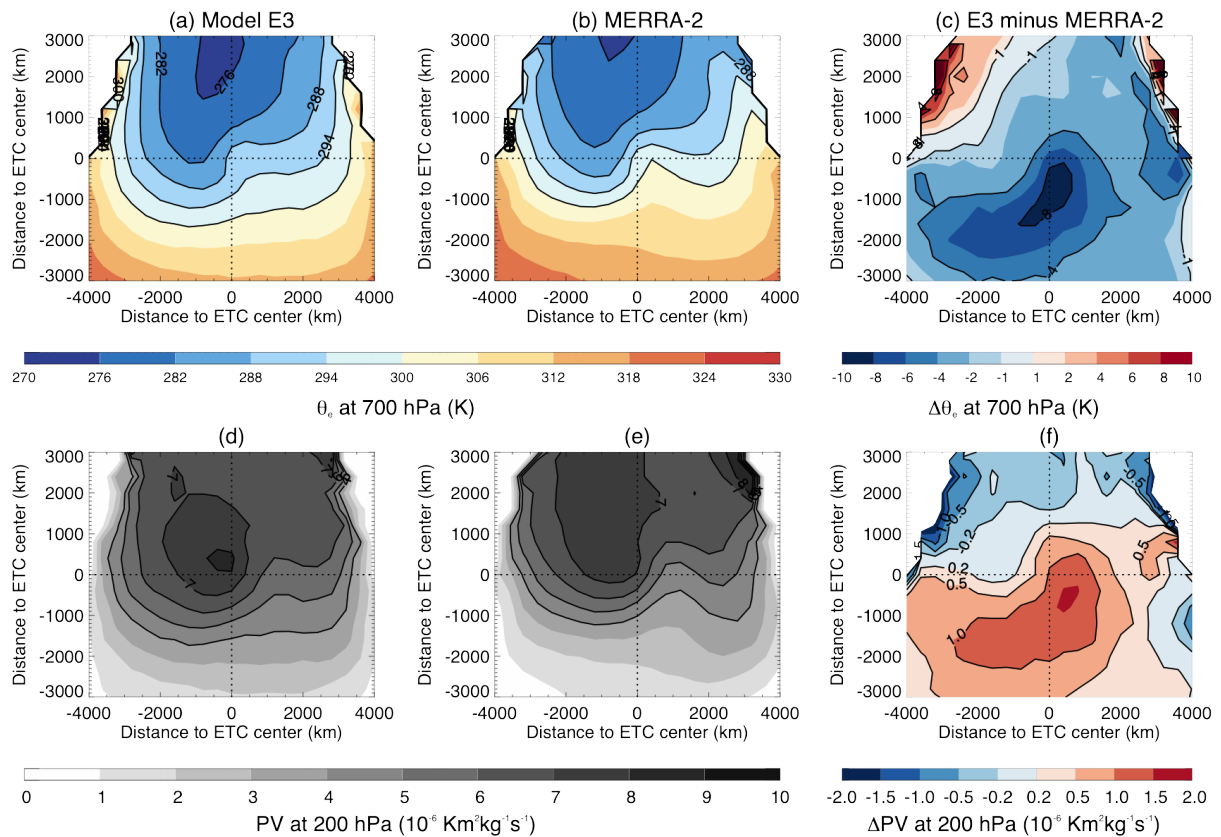
358 relatively large values, reflecting the location of the warm and moist air stream that wraps itself
 359 cyclonically around the cyclone center (Figure 4a). Joining the inflection points of each θ_e
 360 contour establishes the general location of the OTR (dashed blue line). The vertical transect
 361 perpendicular to the ridge (A-B line in Figure 4a) reveals the presence of a poleward sloping axis
 362 of maximum θ_e that coincides with a strong ascent, both typical of the thermal ridge (Figure 4b;
 363 c.f. Martin 1998a).
 364



365
 366 Figure 4: An exemplar of an occluded cyclone simulated in E3 centered at 58.06° N and
 367 149.91° W. (a) Plan view of the sea level pressure field (dashed contour, from 970 hPa in 4hPa
 368 increments), and the 700 hPa equivalent potential temperature (θ_e) field (solid red, from 270 K,
 369 in 3K increments), with the dashed blue line representing the OTR at 700 hPa and the solid black
 370 line representing a transect from A to B perpendicular to the thermal ridge with an intersect at R;
 371 (b) the vertical transects from A to B along the perpendicular to the ridge of θ_e (red contours,
 372 from 260 K, in 6K increments) and vertical velocity where ascending (blue contours, from -45
 373 hPa/hr, in 5 hPa/hr increments) as a function of the distance to the ridge intersect at 700 hPa (R)
 374 in 200 km increments. The vertical dotted line indicates the location of the ridge at 700 hPa.
 375

376 To assess whether this example is representative of most occlusions in E3, we build
 377 cyclone-centered, plan-view composites of 700 hPa θ_e for all DJF NH cyclones with a center over
 378 the ocean in E3 and MERRA-2, along with similarly constructed composites of the potential
 379 vorticity at 200 hPa (Figure 5). These composites are constructed only for the time of maximum
 380 intensity during occlusion – that is, when any given occluded cyclone experiences its lowest sea
 381 level pressure. This is to avoid analysis issues that might arise from differing occlusion
 382 longevities (c.f. Fig. 3b) and to ensure both sets of cyclones are as representative of a typical

383 occlusion as possible. Because of topography, both cyclone tracking and occlusion identification
 384 algorithms may yield artifacts and result in larger uncertainties over land. Furthermore, the
 385 representation of topography in models is affected by the underlying spatial resolution.
 386 Therefore, from this point forward, E3's evaluation only considers the subset of cyclones whose
 387 centers reside over *open ocean*.
 388



389
 390 Figure 5: Cyclone-centered composites of (a,b) equivalent potential temperature at 700 hPa
 391 in Model E3 and MERRA-2 respectively, with (c) the difference between the two; and of (d,e)
 392 200 hPa potential vorticity for Model E3 and MERRA-2 with (f) the difference between E3 and
 393 reanalysis. The dotted lines intersect at the cyclone center.
 394

395 The 700 hPa θ_e composites show the typical contrast between the warm moist southerly
 396 flow and the cold dry northerly flow, with a sharp gradient at the cyclone center and a tongue of
 397 relatively higher θ_e expanding from southeast to northwest just east of the cyclone center, i.e.
 398 the thermal ridge. While Model E3 realistically represents the overall thermal structure of the

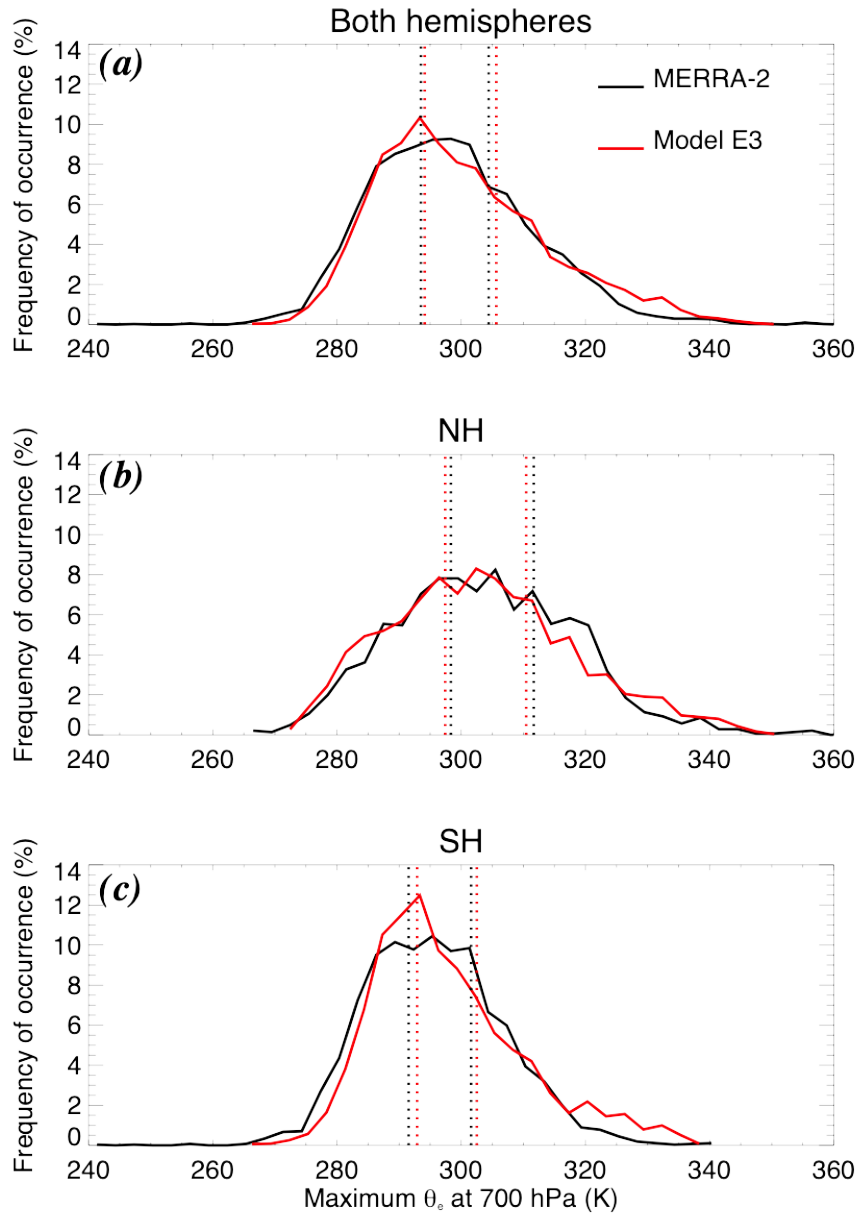
399 occluded cyclones at their peak intensity, the simulated cyclones have lower θ_e values at the
400 center and less well defined thermal ridges (Fig. 5a versus 5b; Fig. 5c).

401 The cyclone-centered composites of potential vorticity (PV) reveal a sharp gradient from
402 west to east across the cyclone center, with a maximum in PV just to the northwest of the
403 cyclone center and a tongue of relatively low PV to the east. Previous research has
404 demonstrated that strong latent heat release in the thermal ridge erodes the relatively high PV
405 region in that vicinity, leading to the development of a low PV trough there (Martin 1998a,
406 Posselt and Martin, 2004). As described in Martin (1998a), in individual cyclones, the PV
407 maximum close to the cyclone center is connected to a high PV reservoir at higher latitudes
408 through a narrow filament making the PV distribution resemble a treble clef structure. Such a
409 structure could be seen for randomly selected cyclones (not shown), however, in the MERRA-2
410 composite the filaments do not align across all cyclones, smearing the treble clef pattern,
411 resulting in a relatively wide area of high PV expanding poleward from just northwest of the
412 cyclone center instead (Fig. 5e). While the E3 composite of PV (Fig. 5d) shares similarities with
413 that from MERRA-2, the PV trough to the east of the cyclone center, like the simulated 700 hPa
414 θ_e thermal ridge in Fig. 5a, is less well defined. Therefore, while the model provides a realistic
415 thermal and kinematic structure at both lower- and upper-levels respectively, the composite
416 differences compel further examination of the thermal ridge, with a focus on clouds.

417 *c. How well are thermal, kinematic and moisture variables represented in the E3 thermal ridge?*

418 To examine the thermal ridge structure, we construct and analyze vertical transect
419 composites across the thermal ridge as described in Section 2e. Discrepancies in the statistical
420 location of the occluded cyclones in E3 relative to MERRA-2 cause differences in the mean
421 cyclone-centered θ_e and PV distributions that tie more to mean state climatology mis-
422 representation and less to cyclone-specific feature differences. To better judge whether the
423 vertical structure of the OTR is well represented in the model, we elect to conduct the ridge
424 comparison between E3 and reanalysis for similar cyclones. To begin, we sort all occluded
425 cyclones according to their $\max(\theta_e)$ at 700 hPa along the thermal ridge. In this manner, we
426 facilitate a fairer comparison of the E3 composite transects of θ_e and ω with MERRA-2 for
427 similar thermal ridges. This is achieved by dividing the entire population of thermal ridges into

428 three equal size subsets, using the same $\max(\theta_e)$ thresholds for both the model and reanalysis.
 429 A sufficient sample size per $\max(\theta_e)$ category is afforded by expanding the analysis of maritime
 430 cyclones to include both hemispheres and all seasons.
 431

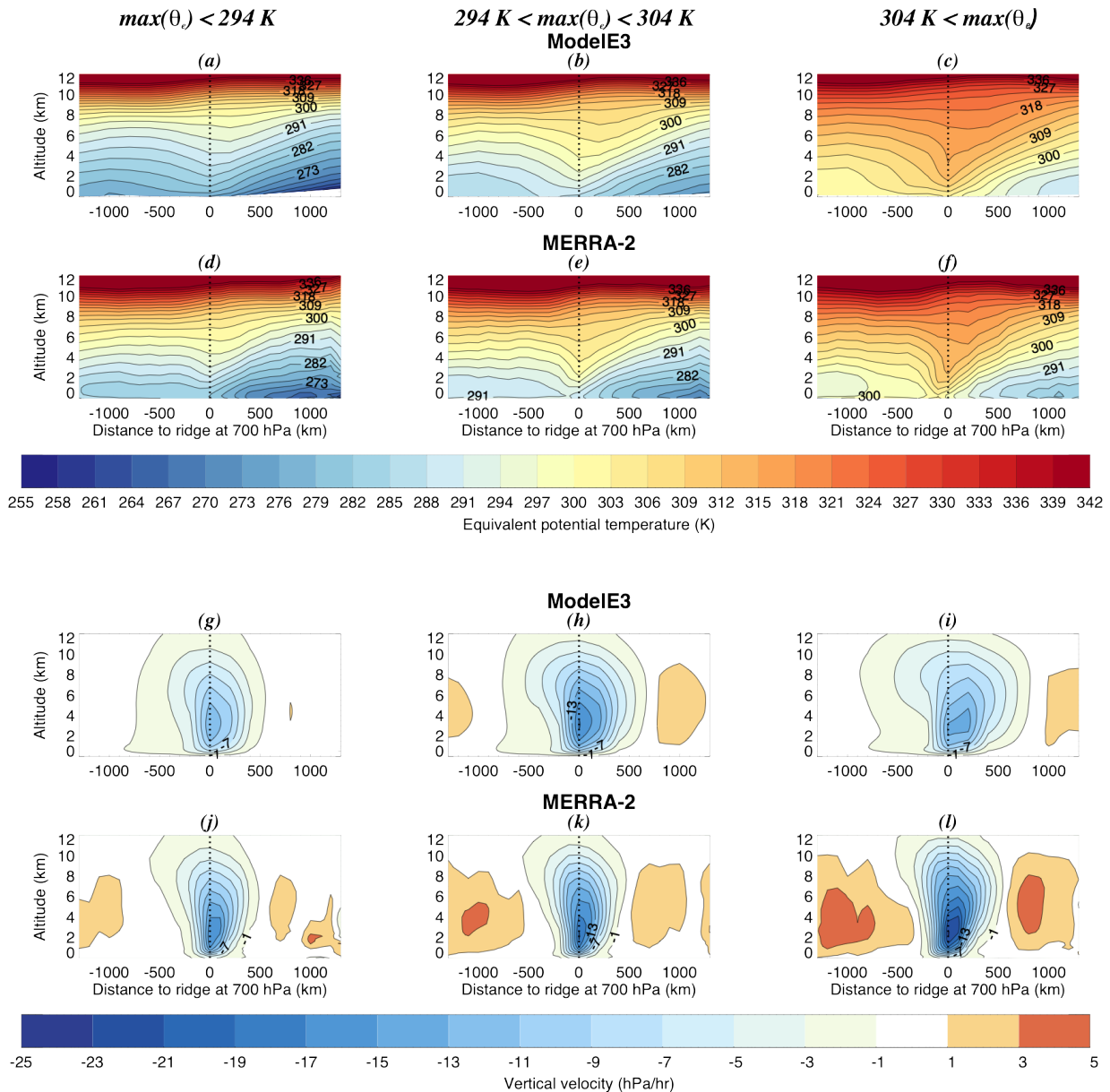


432
 433 Figure 6: Distribution of $\max(\theta_e)$ at 700 hPa in all thermal ridges for all seasons in (a) both
 434 hemispheres, (b) in the northern hemisphere only and (c) in the southern hemisphere only, for
 435 MERRA-2 (black) and Model E3 (red). The dotted lines indicate the θ_e values that divide the
 436 populations into three equal size subsets (red for Model E3, black for MERRA-2).
 437

438 Next, we use CloudSat-CALIPSO overpasses of thermal ridges to obtain an independent
439 view of hydrometeors across thermal ridges. The narrow swath of the instruments means that
440 only a subset of all thermal ridges can be observed. To overcome this limitation, we use the full
441 2006-2017 period with observations to ensure a large enough sample size in our reference
442 dataset. Since the model provides complete information for all thermal ridges, for E3, we
443 investigate the same 5-year dataset used in earlier described analyses. We find that both E3 and
444 the expanded observational dataset (MERRA-2 occlusions with a CloudSat-CALIPSO overpasses)
445 share a very similar distribution of $\max(\theta_e)$ at 700 hPa across all OTRs (Figure 6a), with slightly
446 cooler cases in E3 for the NH (Fig 6b) and warmer ones for the Southern Hemisphere (Fig 6c)
447 relative to MERRA-2. Using the entire population, the three $\max(\theta_e)$ categories are defined as
448 ridges with 1) $\theta_e < 294$ K, 2) $294 < \theta_e < 304$ K, and 3) $\theta_e > 304$ K. These are the categories we
449 anchor against for all the thermal ridge transect comparisons.

450 Composite transects of θ_e and vertical velocity (ω) across the thermal ridge (Figure 7)
451 confirm that the single case of Figure 4 is representative of general E3 OTR structure. For each
452 $\max(\theta_e)$ category, E3 thermal structures across the thermal ridge are realistic, albeit not as well
453 defined as their MERRA-2 counterparts, with E3 simulating comparable variation in θ_e transects
454 from one $\max(\theta_e)$ category to the next. The “warmest” category exhibits the closest match to
455 the canonical structure of a warm occluded thermal ridge as discussed in Naud et al. (2023) and
456 it is realistically represented by E3 (Fig. 7c versus 7f).

457 While E3 is also comparable to MERRA-2 with respect to ω , with a maximum slightly
458 poleward of the thermal ridge, a clear vertical expansion and increased tilt with increasing
459 $\max(\theta_e)$, the maximum in ascent strength is lower in the model, with differences in maximum
460 ω at the ridge of at least 2 hPa/hr (for the coldest $\max(\theta_e)$ category, Fig. 7g vs. 7j). This may be
461 due to the coarser spatial resolution of E3 compared to MERRA-2. However, the reanalysis
462 indicates that vertical velocities are the strongest for the warmest $\max(\theta_e)$ category, while the
463 model produces the greatest ascent strength for the medium $\max(\theta_e)$ category. To test whether
464 this discrepancy might have consequences for clouds and precipitation in the thermal ridge,
465 which in turn would affect latent heat release as well as its impact on occlusion persistence and
466 overall evolution, we next examine composite transects of cloud fraction.



469 Figure 7: Composite transects across the thermal ridge of (a-f) θ_e and (g-l) vertical velocity
 470 for ModelE3 (a-c, g-i) and MERRA-2 (d-f, j-l) for three categories from (a,d,g,j) $\theta_e < 294$ K,
 471 (b,e,h,k) $294 < \theta_e < 304$ K and (c,f,i,l) $\theta_e > 304$ K. In each subplot, the vertical dashed line marks
 472 the location of the thermal ridge at 700 hPa, the x-axis is the distance to the ridge (in km), and
 473 the y-axis the altitude (in km).
 474

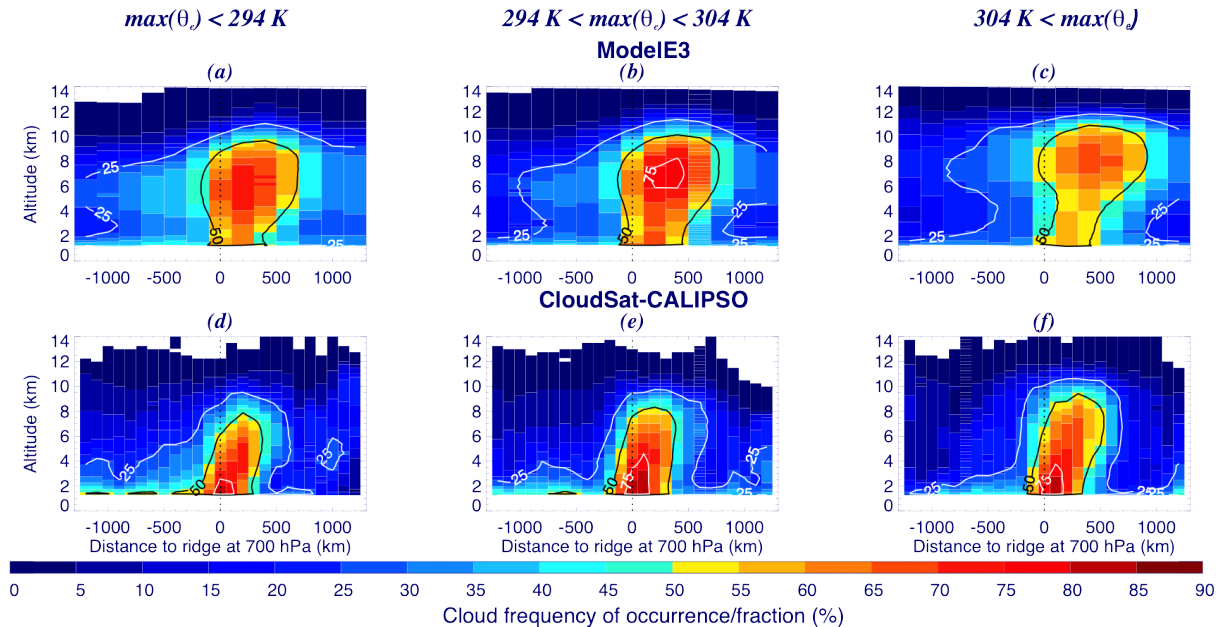
475 Using Model E3 profiles of cloud fraction, we build composite transects following the same
 476 method used for θ_e and ω transects. The model cloud fraction is computed as the sum of

477 convective and stratiform cloud fraction (including precipitation fraction) as viewed by the
478 model radiation scheme. As discussed previously, the observed profiles are not evenly
479 distributed in space, and instead are provided along the satellite's orbit (c.f. Section 2e; Naud et
480 al., 2024). Therefore we only sample some portion of the thermal ridge area for each case. In
481 Naud et al. (2024), it is shown that by compositing multiple cases the impact of this sparse
482 coverage can be alleviated. The observation-based composite transects are the sum of all
483 observed profiles of the hydrometeor mask (with 1s where GEOPROF-LIDAR indicates a cloud
484 layer, 0s otherwise) normalized by the total number of profiles. The result is a frequency of
485 hydrometeor occurrence across the thermal ridge. Some differences between E3 and
486 observations can arise due to precipitation contamination in the observations attenuating radar
487 signals to such an extent that hydrometeors at lower altitudes are not observable.

488 Figure 8 shows the composite transects of E3 cloud fraction per $\max(\theta_e)$ category and the
489 corresponding transects of hydrometeor frequency of occurrence obtained from CloudSat-
490 CALIPSO. Regarding simulated versus observed hydrometeor transects for each $\max(\theta_e)$
491 category independently, E3 exhibits larger cloud fractions above 8 km than observed along with
492 a tendency to expand further poleward at those altitudes as well. This is true for all three
493 $\max(\theta_e)$ categories. At those altitudes, the CALIPSO lidar is less often attenuated and the
494 observations are quite accurate as a result. Therefore, it is probable that the E3 overestimation
495 of cloud fraction (by at least 5-10%) is a robust result at those higher altitudes. In contrast to the
496 higher altitude results, CloudSat-CALIPSO displays a maximum in hydrometeor frequency at low
497 altitudes (below 5 km), where only the radar can sense hydrometeors, and where precipitating
498 hydrometeors tend to be more frequent.

499 Despite these differences in overall distribution, the model does reproduce the contrasts
500 between $\max(\theta_e)$ categories in accord with observations: cloud tops expand upward and
501 poleward from low to high θ_e categories. As previously reported in Naud et al. (2024) for the
502 observations, the maximum in cloud fraction in the largest θ_e category is less than that of the
503 middle θ_e category. However, the drop in maximum cloud fraction from medium to high $\max(\theta_e)$
504 ridges is more dramatic in E3 than observed (in fact it is barely noticeable in the observed

505 transects), which is possibly exacerbated by the concurrent drop in ascent strength that only E3
 506 produces.
 507



508
 509 Figure 8: Composite transect of model E3 cloud fraction (a-c) across the thermal ridge for
 510 three θ_e categories, and corresponding transects of CloudSat-CALIPSO cloud frequency of
 511 occurrence (d-f). (a,d) include thermal ridges with θ_e at 700 hPa $< 294\text{K}$, (b, e) $294 < \theta_e < 304\text{K}$,
 512 and (c,f) $304\text{K} < \theta_e$. In each panel, the vertical dotted line indicates the location of the thermal
 513 ridge, and the solid black and white contours the 25, 50 and 75% fraction/frequency levels.
 514

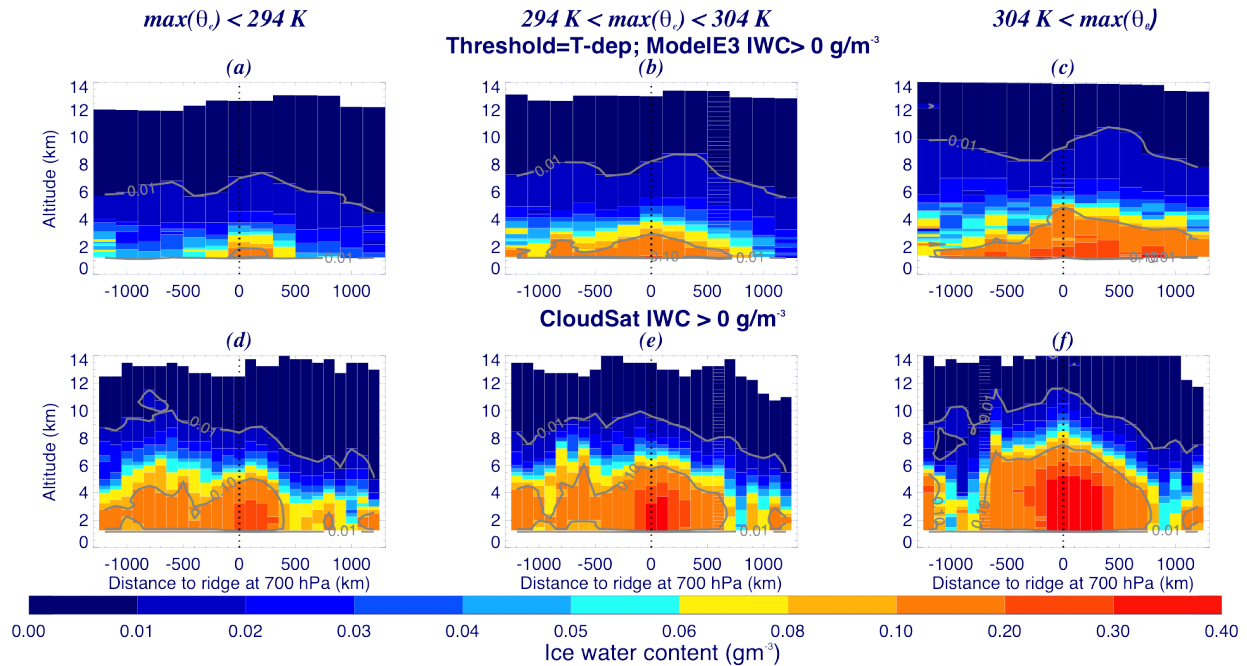
515 Because cloud fraction only describes where and when clouds form, it does not relay
 516 information regarding how tenuous those clouds might be. Therefore, we analyze a different
 517 diagnostic of the cloud state: composite transects of ice water content. These data are provided
 518 by the 2C-ICE product, and we utilize the same compositing strategy as that used for
 519 hydrometeor frequency, i.e. the vertical profiles of hydrometeor presence/absence are replaced
 520 with profiles of ice water content. To separate out the impact of changing hydrometeor
 521 frequency from one $\max(\theta_e)$ category to the next, ice water content is only averaged where ice
 522 is present, i.e. $\text{IWC} > 0\text{ gm}^{-3}$. Because 2C-ICE relies on a combination of information from both
 523 lidar and radar, greater uncertainties are expected in cloud areas where only one of the two
 524 instruments can detect hydrometeors. The lidar signal is superior at detecting small particles
 525 often found near cloud top that the radar cannot detect, and inversely, the lidar signal gets

526 attenuated in thick clouds leaving radar reflectivities solely available at lower altitudes (Deng et
527 al., 2010). Profiles of E3 IWC are composited with the same method used for the other
528 variables, as described, but after a re-set of IWC to zero if below the thresholds discussed in
529 Section 2d. The model provides ice mass for both stratiform and convective cloud, including
530 precipitating components. Here we use the sum of all four components.

531 For each $\max(\theta_e)$ category, Model E3 simulates lower values of IWC than reported from 2C-
532 ICE (Figure 9). However, the overall distribution of IWC with altitude exhibits a more realistic
533 pattern than the cloud fraction, with larger mass at lower rather than higher altitudes, as would
534 be expected in environments where available moisture is maximized at lower levels. Below the
535 50% model cloud occurrence level (c.f. at levels below the solid black line in Fig. 8a, b, c), while
536 the model reproduces the variations in IWC across the ridge, with a maximum at and poleward
537 of the ridge, the overall magnitude is less than observed. This implies that E3 produces clouds
538 too often but with less ice than observed. This “too many, too tenuous” high-level cloud bias is
539 in contrast to what has often been reported in most ESM analyses at lower altitudes: the “too
540 few, too bright” cloud problem (e.g. Nam et al., 2012; Konsta et al., 2022). At lower altitudes
541 with a temperature range where mixed phases occur, biases could be reflective of differences in
542 temperature thresholds for assumed ice – liquid partitioning in CloudSat-CALIPSO versus the
543 GISS model: for the latter, liquid extends to colder temperatures, thus lower ice cloud fractions.

544 For occlusions in general, simulated and observed transects reveal a clear increase in IWC
545 from low to medium to high $\max(\theta_e)$ thermal ridges. Therefore, while the “warmest” thermal
546 ridges may have less frequent clouds than their slightly “cooler” counterparts, they do contain
547 more ice, which is consistent with larger precipitation rates as reported in Naud et al. (2024).
548 Remarkably, the model represents these contrasts well, lending confidence that it reproduces
549 the moist processes in these occluded systems in a fairly realistic way. However, the lower IWC
550 overall implies insufficient modeled latent heating, which could contribute to the weaker PV
551 erosion aloft, and possibly the lower overall occurrence of occlusions.

552



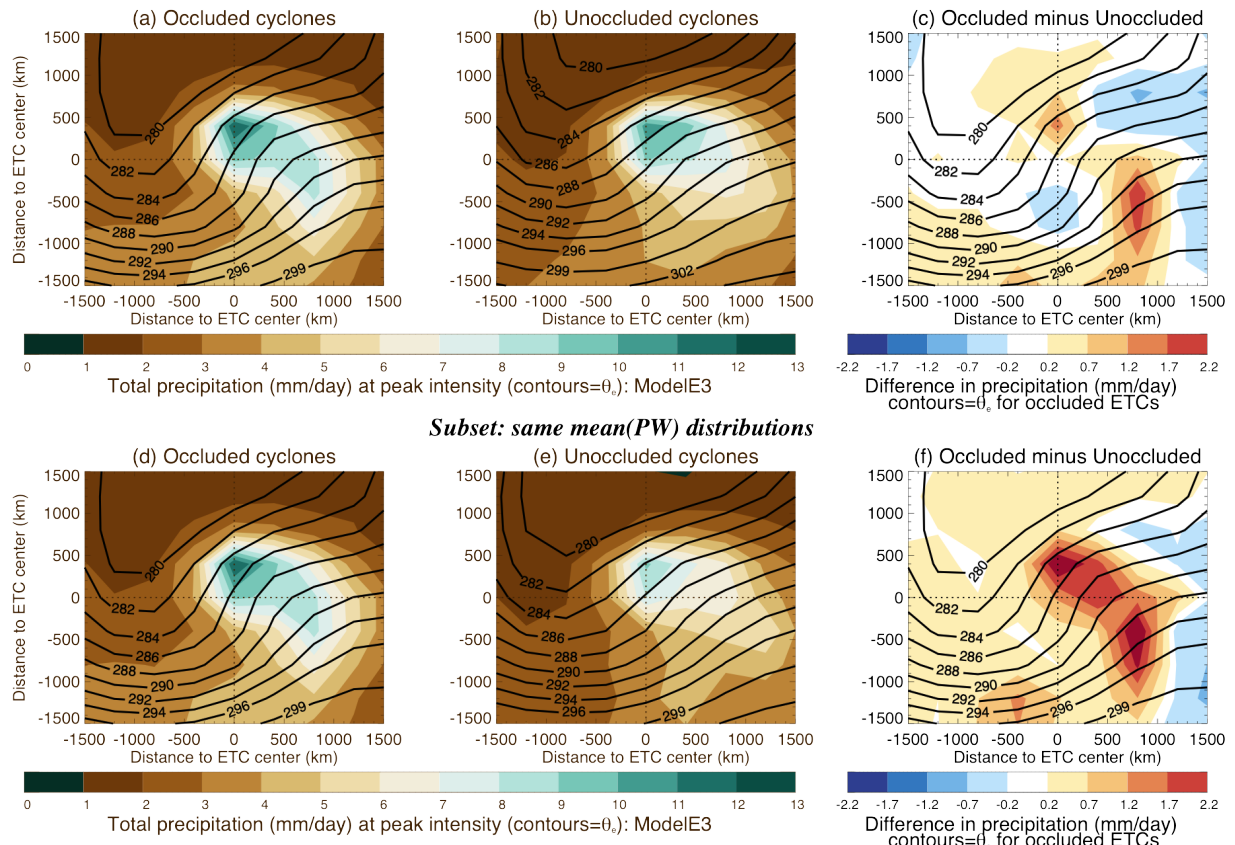
553

554 Figure 9: Composite transects of conditional IWC (i.e, average over all scenes for IWC > 0)
 555 from (a-c) Model E3, and (d-f) CloudSat-CALIPSO (2C-ICE) for the three thermal ridge
 556 categories: (a, d) $\max(\theta_e) < 294 \text{ K}$, (b, e) $294 < \max(\theta_e) < 304$ and (c, f) $304 \text{ K} < \max(\theta_e)$. In each
 557 panel the vertical dashed line represents the location of the thermal ridge at 700 hPa. The light
 558 grey contours show the 0.01 and 0.1 gm^{-3} IWC levels.

559 4. Discussion

560 Analyses thus far have verified that 1) an ESM can produce occluded cyclones, 2) it does so
 561 with realistic thermal and kinematic structures, but 3) with some possible biases in the
 562 representation of ascent strength, cloud coverage and ice mass. While these issues may connect
 563 to the number of occluded cyclones, their location and their longevity, they do not impair the
 564 ability of the model to represent a realistic sensitivity of clouds in the thermal ridge to the
 565 thermodynamic characteristics of the thermal ridge. However, we have not demonstrated the
 566 importance of this ability in a climatological context and why further improvements in the
 567 simulation of clouds and precipitation in the model are necessary. To this end, we begin by
 568 exploring the mean precipitation in E3 cyclones that have reached their peak intensity –
 569 separating such cyclones into those that, at some point in their life cycles, occlude, and those
 570 that never do (according to the identification method outlined in Section 2d). One caveat is that
 571 the occlusion identification method is conservative. It is designed to excel at identifying cyclones

572 that are occluded, but tends to reject ambiguous cases. Therefore, a small number of cyclones
 573 at peak intensity categorized as “unoccluded” may arguably be occluded.
 574



575
 576 Figure 10: Cyclone-centered composites of E3 surface precipitation rates (in color) for (a)
 577 occluded cyclones and (b) unoccluded cyclones at peak intensity, with solid contour showing
 578 their associated composite of equivalent potential temperature (in 2K intervals from 280 K) . (c)
 579 Difference in precipitation between occluded and unoccluded cyclones, with solid contours
 580 showing the composite of equivalent potential temperature of occluded cyclones. (d, e, f) show
 581 similar composites to (a, b, c) but for a subset of cyclones at peak intensity for which both
 582 occluded and unoccluded subsets share the same distribution of mean(PW) across cyclones. The
 583 dotted lines intersect at the cyclone’s center.
 584

585 Cyclone-centered composites of surface precipitation are constructed for each subset of
 586 cyclones (Fig. 10a-b). These composites reveal that in E3, cyclones that do occlude produce
 587 more precipitation than those that do not, with differences up to 1.5-2 mm/day at the locations
 588 where cyclones in general produce most of the precipitation (Figure 10c), i.e., northwest of the
 589 cyclone center (i.e. the TROWAL region), and the pre-cold frontal (warm sector) region.

590 However, further analysis revealed that the set of unoccluded cyclones include a greater
591 fraction of systems with large mean precipitable water (PW) in their environments (22% have
592 PW > 13 mm, compared to 6% of occluded cyclones). This is likely related to the tendency for E3
593 occluded cyclones to occur frequently at high latitudes, away from the high PW reservoir, while
594 unoccluded cyclones have a more widespread latitude distribution. PW and precipitation are
595 highly correlated in cyclones (e.g. Field and Wood, 2007; Booth et al. 2018; Sinclair and Catto,
596 2023), thus we sort the two sets of cyclones to force the mean cyclone-wide PW distribution
597 across all cyclones in each subset to match. This is achieved by randomly removing cyclones
598 from each set until both sets include the same number of cyclones with a given mean PW
599 within 1 mm. For these two sets of occluded and unoccluded cyclones with matching PW
600 distributions, the difference in precipitation is much larger, as might be expected, but not
601 previously documented (Figure 10d-f). This suggests that E3 occluded cyclones are more
602 efficient at processing PW into precipitation. Preliminary tests made using a similar stratification
603 of precipitation observations (not shown) confirm that occluded cyclones are, indeed, more
604 efficient at precipitation production. The full details of this analysis will be presented in a
605 forthcoming paper. This result demonstrates that occluded cyclones play an important role in
606 the production of precipitation and its extremes, and that ESMs must faithfully reproduce this
607 stage in the cyclone life cycle to accurately represent precipitation totals, their future changes
608 and their extremes.

609 **5. Conclusions**

610 Using a novel method for identifying extratropical cyclones that undergo an occlusion, the
611 most recent version of the GISS Earth System Model (E3) was tested for its ability to represent
612 occlusions, their structure and their associated cloud field. Though Model E3 can simulate the
613 occlusion process, compared to the MERRA-2 reanalysis it tends to 1) underestimate the
614 number of tracks with occlusion, 2) place the occlusions too far poleward and 3) simulate long-
615 duration occlusions too often. However, the thermal and kinematic structure of the model's
616 occluded cyclones and attendant thermal ridges are reasonably well depicted. An analysis of
617 CloudSat-CALIPSO GEOPROF-LIDAR hydrometeor retrievals against E3 reveals that the E3 cloud
618 distribution across thermal ridges, while displaying a reasonable sensitivity to the thermal ridge

619 characteristics, tends to be top-heavy, i.e. the model has a tendency to produce high clouds too
620 frequently and over a wider area than suggested by satellite data. When ice water content
621 transects are compared to CloudSat-CALIPSO 2C-ICE retrievals, a more realistic vertical
622 distribution of condensate amounts is produced by E3, albeit with less ice than observed. This
623 issue of “too many, too tenuous” high-level clouds is not unique to E3 (e.g. Naud et al., 2019),
624 and should inform needed model developments as modelling centers prepare for CMIP7.

625 Further work will be necessary to establish the root cause of this issue, which could be
626 conducted by using the other members of the Calibrated Physics ensemble developed for E3
627 (Elsaesser et al., 2024). In the ensemble, the physics is the same across models, but the various
628 parameters used for tuning are not. An intercomparison of the different members could help
629 establish whether these issues stem from the tuning parameter settings. Also, known issues in
630 E3’s parameterization schemes could impact cloud fraction and ice amounts at high altitudes in
631 thermal ridges: 1) a too-weak sink term of stratiform anvil cloud area (possibly arising from
632 insufficient IWC seeding stratiform rainfall; Elsaesser et al., 2022) and 2) an overactive
633 detrainment of slowly-sedimenting small-ice particles from any embedded convective clouds
634 (e.g., Elsaesser et al. 2017a).

635 Extratropical cyclones need to be well-represented in ESMs because of their important role
636 in the meridional transport of heat and moisture, as well as in the production of precipitation,
637 and its extremes. Here, using E3 cyclone-centered precipitation, we demonstrate that the *life*
638 *cycle* of these systems also requires adequate representation because occluded cyclones in the
639 model are a lot more efficient at converting moisture into precipitation compared to cyclones
640 that never occlude. The next step will be to use E3 to explore occluded cyclones in a warmer
641 climate with the goal of quantifying how an increased global temperature might influence the
642 occlusion process and associated precipitation. As the resolution and sophistication of ESMs
643 increase, the impact of microphysical processes on occlusions and how they might be
644 represented in models will also benefit from increased scrutiny. Such efforts will be aided by
645 adding more vertically-resolved observations and improved IWC and particle size measurements
646 in general, such as those jointly retrieved from the radar and microwave radiometer aboard
647 GPM, retrievals from in-development ice-sensing satellite missions (e.g., the Polarized

648 Submillimeter Ice-cloud Radiometer – PolSIR - sampling the most equatorward cyclone-
649 associated ice clouds), and radar and lidar data from the European Space Agency Earth Cloud
650 Aerosol and Radiation Explorer mission (EarthCARE; Illingworth et al., 2015).

651

652 *Acknowledgments.*

653 The work was funded by the NASA CloudSat-CALIPSO science team recompute program,
654 grant number 80NSSC20K0085. CMN and DJP received additional funding from the NASA
655 Modeling, Analysis and Prediction (MAP) program, grant number 80NSSC21K1728 and GSE
656 from the NASA MAP Program and APAM-GISS Cooperative Agreement 80NSSC18M0133,
657 NASA Precipitation Measurement Missions grant 80NSSC22K0609, and the NASA PolSIR
658 project (80LARC24CA001). A portion of this research was conducted at the Jet Propulsion
659 Laboratory, California Institute of Technology, under a contract with the National Aeronautics
660 and Space Administration (NASA) 80NM0018D0004. Computing resources for the work were
661 provided by the NASA High-End Computing (HEC) program through the NASA Center for
662 Climate Simulation (NCCS) at the Goddard Space Flight Center. The authors thank Min Deng
663 and Matthew Lebsock for detailed information on CloudSat and CALIPSO measurements and
664 products, and three anonymous reviewer for their insightful comments that greatly helped
665 improve this manuscript.

666

667 *Data Availability Statement.*

668 The MERRA-2 database of occluded cyclones and the ERA-Interim database of cyclones are
669 accessible here: <https://data.giss.nasa.gov/storms/obs-etc/>.

670 CloudSat-CALIPSO 2B-GEOPROF-LIDAR and 2C-ICE data files are documented and available here:
671 <https://www.cloudsat.cira.colostate.edu/>.

672 MERRA-2 profiles of temperature, specific humidity, wind and vertical velocity information are
673 available here:

674 Global Modeling and Assimilation Office (GMAO) (2015), MERRA-2 inst3_3d_asm_Np: 3d,3-
675 Hourly,Instantaneous,Pressure-Level,Assimilation,Assimilated Meteorological Fields V5.12.4,

676 Greenbelt, MD, USA, Goddard Earth Sciences Data and Information Services Center (GES DISC),
677 Accessed: 2020-01, [10.5067/QBZ6MG944HW0](https://doi.org/10.5067/QBZ6MG944HW0)
678 Global Modeling and Assimilation Office (GMAO) (2015), MERRA-2 inst6_3d_ana_Np: 3d,6-
679 Hourly,Instantaneous,Pressure-Level,Analysis,Analyzed Meteorological Fields V5.12.4,
680 Greenbelt, MD, USA, Goddard Earth Sciences Data and Information Services Center (GES DISC),
681 Accessed: 2020-01, [10.5067/A7S6XP56VZWS](https://doi.org/10.5067/A7S6XP56VZWS).

682 REFERENCES

- 683 Bauer, M. and A. D. Del Genio, 2006: Composite analysis of winter cyclones in a GCM: Influence
684 on climatological humidity. *J. Climate*, 19, 1652-1672.
- 685 Bauer M., G. Tselioudis and, W. B. Rossow, 2016: A new climatology for investigating storm
686 influences in and on the extratropics. *J. Appl. Meteorol. Clim.* 55 1287–303
- 687 Bengtsson L., K. I. Hodges, and N. Keenlyside, 2009: Will extratropical storms intensify in a
688 warmer climate? *J. Climate*, 22, 2276-2301, doi:10.1175/2008JCLI2678.1.
- 689 Binder, H., Boettcher, M., Joos, H. and Wernli, H. (2016) The role of warm conveyor belts for the
690 intensification of extratropical cyclones in Northern Hemisphere winter. *Journal of the*
691 *Atmospheric Sciences*, 73, 3997–4020
- 692 Bjerknes, J., and H. Solberg, 1922: Life cycle of cyclones and the polar front theory of
693 atmospheric circulation. *Geophys. Publ.*, 3 (1), 1–18.
- 694 Booth J. F., C. M. Naud, J. Willison, 2018: Evaluation of Extratropical Cyclone Precipitation in the
695 North Atlantic Basin: An analysis of ERA-Interim, WRF, and two CMIP5 models. *J. Climate*,
696 31:6, 2345-2360.
- 697 Bretherton, C. S., and S. Park, 2009: A new moist turbulence parameterization in the community
698 Atmosphere Model. *J. Climate*, 22, 3422-3448.
- 699 Catto, J. L., C. Jakob, G. Berry and N. Nicholls 2012: Relating global precipitation to atmospheric
700 fronts. *Geophys. Res. Lett.*, 39, L10805, doi: 10.1029/2012GL051736.
- 701 Catto, J. L., C. Jakob, and N. Nicholls, 2015: Can the CMIP5 models represent winter frontal
702 precipitation? *Geophys. Res. Lett.*, 42, 8596-8604, doi:10.1002/GL2015GL066015.

703 Cesana, G., A.D. Del Genio, A.S. Ackerman, M. Kelley, G. Elsaesser, A.M. Fridlind, Y. Cheng, and
704 M.-S. Yao, 2019: Evaluating models' response of tropical low clouds to SST forcings using
705 CALIPSO observations. *Atmos. Chem. Phys.*, **19**, 2813-2832, doi:10.5194/acp-19-2813-2019.

706 Cesana, G. V., A. S. Ackerman, A. M. Fridlind, I. Silber, and M. Kelley, 2021: Snow reconciles
707 observed and simulated phase partitioning and increases cloud feedback. *Geophysical*
708 *Research Letters*, **48**, e2021GL094876. <https://doi.org/10.1029/2021GL094876>.

709 Cheng, Y., V.M. Canuto, A.M. Howard, A.S. Ackerman, M. Kelley, A.M. Fridlind, G.A. Schmidt,
710 M.S. Yao, A. Del Genio, and G.S. Elsaesser, 2020: A second-order closure turbulence model:
711 New heat flux equations and no critical Richardson number. *J. Atmos. Sci.*, **77**, no. 8, 2743-
712 2759, doi:10.1175/JAS-D-19-0240.1.

713 Crocker, A., W. L. Godson, and C. M. Penner, 1947: Frontal contour charts. *J. Atmos. Sci.*, **4** (**3**),
714 95–99.

715 Dee D. P., and co-authors., 2011: The ERA-Interim reanalysis: configuration and performance of
716 the data assimilation systems. *Quart. J. R. Meteorol. Soc.*, **137**, 553-597.

717 Del Genio, A.D., J. Wu, A.B. Wolf, Y.H. Chen, M.-S. Yao, and D. Kim, 2015: Constraints on cumulus
718 parameterization from simulations of observed MJO events. *J. Climate*, **28**, no. 16, 6419-
719 6442, doi:10.1175/JCLI-D-14-00832.1.

720 Deng, M., G. G. Mace, Z. Wang, and H. Okamoto, 2010: Tropical Composition, Cloud and Climate
721 Coupling Experiment validation for cirrus cloud profiling retrieval using CloudSat radar and
722 CALIPSO lidar, *J. Geophys. Res.*, **115**, D00J15, doi:10.1029/2009JD013104 (6)

723 Deng M, Gerald G. Mace, Zhen Wang, and R. Paul Lawson, 2013: Evaluation of Several A-Train
724 Ice Cloud Retrieval Products with In Situ Measurements Collected during the SPARTICUS
725 Campaign. *J. Appl. Meteor. Climatol.*, **52**, 1014–1030.

726 Elsaesser, G.S., A.D. Del Genio, J. Jiang, and M. van Lier-Walqui, 2017a: An improved convective
727 ice parameterization for the NASA GISS Global Climate Model and impacts on cloud ice
728 simulation. *J. Climate*, **30**, no. 1, 317-336, doi:10.1175/JCLI-D-16-0346.1.

729 Elsaesser, G. S., M. van Lier-Walqui, Q. Yang, M. Kelley, A. S. Ackerman, A. M. Fridlind, G. V.
730 Cesana, G. A. Schmidt, J. Wu, A. Behrangi, S. J. Camargo, B. De, K. Inoue, N. Leitmann-Niimi,

731 and J. D. O. Strong, 2024: Using Machine Learning to generate a GISS ModelE Calibrated
732 Physics Ensemble (CPE). Submitted to J. Adv. Model. Earth Syst..

733 Elsaesser, G.S., C.W. O'Dell, M.D. Lebsock, R. Bennartz, and T.J. Greenwald, 2017b: The Multi-
734 Sensor Advanced Climatology of Liquid Water Path (MAC-LWP). *J. Climate*, **30**, no. 24,
735 10193-10210, doi:10.1175/JCLI-D-16-0902.1.

736 Elsaesser, G. S., Roca, R., Fiolleau, T., Del Genio, A. D., & Wu, J. (2022). A simple model for
737 tropical convective cloud shield area growth and decay rates informed by geostationary IR,
738 GPM, and Aqua/AIRS satellite data. *Journal of Geophysical Research: Atmospheres*, **127**,
739 e2021JD035599. <https://doi.org/10.1029/2021JD035599>.

740 Field P. R. and R. Wood, 2007: Precipitation and cloud structure in midlatitude cyclones. *J.*
741 *Climate*, **20**, 233-254, doi:10.1175/JCLI3998.1.

742 Gelaro, R., McCarty, W., Suarez, M. J., Todling, R., Molod, A., Takacs, L., ... Zhao, B. (2017). The
743 Modern-Era Retrospective Analysis for Research and Applications, Version 2 (MERRA-2). *J.*
744 *Climate*, **30(14)**, 5419–5454.

745 Gettelman, A. and Morrison, H., 2015: Advanced Two-Moment Bulk Microphysics for Global
746 Models. Part I: Off-Line Tests and Comparison with Other Schemes, *J. Climate*, **28**, 1268–
747 1287, <https://doi.org/10.1175/JCLI-D-14-00102.1>.

748 Grim J. A., R. M. Rauber, M. K. Ramamurthy, B. F. Jewett and M. Han, 2007: High-resolution
749 observations of the Trowal-Warm-frontal region of two continental winter cyclones. *Month.*
750 *Weath. Rev.*, **135**, 1629-1646, doi:10.1175/MWR3378.1.

751 Han M., R. M. Rauber, M. K. Ramamurthy, B. F. Jewett and J. A. Grim, 2007: Mesoscale dynamics
752 of the TROWAL and warm-frontal regions of two continental winter cyclones. *Month.*
753 *Weath. Rev.* **135**, 1647-1670, doi: 10.1175/MWR3377.1.

754 Hawcroft M. K., L. C. Shaffrey, K. I. Hodges and H. F. Dacre, 2012: How much northern
755 hemisphere precipitation is associated with extratropical cyclones? *Geophys. Res. Lett.*, **39**,
756 L24809, doi:10.1029/2012GL053866.

757 Hoskins B. J. and K. I. Hodges, 2002: New perspectives on the Northern Hemisphere winter
758 storm tracks. *J. Atmos. Sci.*, **59**, 1041–1061.

759 Illingworth A. J. and 28 co-authors, 2015: The EarthCARE satellite: the next step forward in
760 global measurements of clouds, aerosols, precipitation and radiation. *Bull. Amer. Meteorol.*
761 *Soc*, 96, 1311-1332, doi: 10.1175/BAMS-D-12-00227.1.

762 Jewell, R., 1981: Tor Bergeron's first year in the Bergen school: Towards an historical
763 appreciation. *In: Lilequist, G. H. (Ed.) Weather and Weather Maps: a volume dedicated to*
764 *the memory of Tor Bergeron. Vol. 10, Contributions to current research in Geophysics,*
765 *Springer, 474–490.*

766 Kelley, M., G.A. Schmidt, L. Nazarenko, S.E. Bauer, R. Ruedy, G.L. Russell, A.S. Ackerman, I.
767 Aleinov, M. Bauer, R. Bleck, V. Canuto, G. Cesana, Y. Cheng, T.L. Clune, B.I. Cook, C.A. Cruz,
768 A.D. Del Genio, G.S. Elsaesser, G. Faluvegi, N.Y. Kiang, D. Kim, A.A. Lacis, A. Leboissetier, A.N.
769 LeGrande, K.K. Lo, J. Marshall, E.E. Matthews, S. McDermid, K. Mezuman, R.L. Miller, L.T.
770 Murray, V. Oinas, C. Orbe, C. Pérez García-Pando, J.P. Perlwitz, M.J. Puma, D. Rind, A.
771 Romanou, D.T. Shindell, S. Sun, N. Tausnev, K. Tsigaridis, G. Tselioudis, E. Weng, J. Wu, and
772 M.-S. Yao, 2020: GISS-E2.1: Configurations and climatology. *J. Adv. Model. Earth Syst.*, **12**, no.
773 8, e2019MS002025, doi:10.1029/2019MS002025.

774 Konsta, D., Dufresne, J.-L., Chepfer, H., Vial, J., Koshiro, T., Kawai, H., et al., 2022: Low-level
775 marine tropical clouds in six CMIP6 models are too few, too bright but also too compact and
776 too homogeneous. *Geophys. Res. Lett.*, **49**, e2021GL097593. Doi:10.1029/2021GL097593

777 Kunkel K. E., D. R. Easterling, D. A. R. Kristovich, B. Gleason, L. Stoecker and R. Smith, 2012:
778 Meteorological causes of the secular variations in observed extreme precipitation events for
779 the conterminous United States. *J. Hyrometeorol*, 13, 1131-1141, doi:10.1175/JHM-D-11-
780 0108.1.

781 Kunkel K. E. and 24 co-authors, 2013: Monitoring and understanding trends in extreme storms,
782 *Bull. Amer. Meteorol. Soc.*, 94, 499-514, doi: 10.1175/BAMS-D-11-00262.1.

783 Li, J.-L., G. Cesana, K.-M. Xu, M. Richardson, H. Takahashi, and J. Jiang, 2023: Comparisons of
784 simulated radiation, surface wind stress and SST fields over tropical pacific by the GISS
785 CMIP6 versions of global climate models with observations. *Environ. Res. Commun*, **5**,
786 015005.

787 Mace G. G., Q. Zhang, M. Vaughan, R. Marchand, G. Stephens, C. Trepte, and D. Winker, 2009: A
788 description of hydrometeor layer occurrence statistics derived from the first year of merged
789 CloudSat and CALIPSO data. *J. Geophys. Res.*, **114**, D00A26, doi:10.1029/2007JD008755

790 Mace, G. G., and Q. Zhang, 2014: The CloudSat radar-lidar geometrical profile product (RL-
791 GeoProf): Updates, improvements, and selected results, *J. Geophys. Res. Atmos.*, **119**,
792 doi:10.1002/2013JD021374.

793 Marciano C. G., G. M. Lackmann and W. A. Robinson, 2015: Changes in U.S. east coast cyclone
794 dynamics with climate change. *J. Climate*, **28**, 468-484, doi:10.1175/JCLI-D-14-00418.1.

795 Martin, J. E., 1998a: The structure and evolution of a continental winter cyclone. Part I: Frontal
796 structure and the occlusion process. *Mon. Wea. Rev.*, **126** (2), 303–328.

797 Martin, J.E., 1998b: The structure and evolution of a continental winter cyclone. Part II: Frontal
798 forcing of an extreme snow event. *Mon. Wea. Rev.*, **126** (2), 329–348.

799 Martin, J.E., 1999a: Quasi-geostrophic forcing of ascent in the occluded sector of cyclones and
800 the trowal airstream. *Mon. Wea. Rev.*, **127**, 70–88.

801 Martin, J.E., 1999b: The separate roles of geostrophic vorticity and deformation in the mid-
802 latitude occlusion process. *Mon. Wea. Rev.*, **127**, 2404–2418.

803 Nam C., S. Bony, J.-L. Dufresne and H. Chepfer, 2012: The ‘too few, too bright’ tropical low-cloud
804 problem in CMIP5 models. *Geophys. Res. Lett.* **29**(21), doi:10.1029/2012GL063421.

805 Naud, C.M, J.F. Booth, J. Jeyaratnam, L.J. Donner, C.J. Seman, M. Zhao, H. Guo, and Y. Ming,
806 2019: Extratropical cyclone clouds in the GFDL climate model: Diagnosing biases and the
807 associated causes. *J. Climate*, **32**, 6685-6701, doi:10.1175/JCLI-D-19-0421.1.

808 Naud, C.M., P. Ghosh, J.E. Martin, G.S. Elsaesser, and D.J. Posselt, 2024: A CloudSat-CALIPSO
809 view of cloud and precipitation in the occluded quadrants of extratropical cyclones. *Q. J.*
810 *Roy. Meteorol. Soc.*, early on-line, doi:10.1002/qj.4648.

811 Naud, C.M., J. Jeyaratnam, J.F. Booth, M. Zhao, and A. Gettelman, 2020: Evaluation of modeled
812 precipitation in oceanic extratropical cyclones using IMERG. *J. Climate*, **33**, no. 1, 95-113,
813 doi:10.1175/JCLI-D-19-0369.1.

814 Naud, C.M., J.E. Martin, P. Ghosh, G.S. Elsaesser, and D.J. Posselt, 2023: Automated
815 identification of occluded sectors in midlatitude cyclones: Method and some climatological
816 applications. *Q. J. Roy. Meteorol. Soc.*, 149 1990-2010, doi:10.1002/qj.4491.

817 Neu U. and co-authors, 2013: IMILAST, a community effort to intercompare extratropical
818 cyclone detection and tracking algorithms, *Bull. Amer. Meteorol. Soc.*, 94, 529-547,
819 doi:10.1175/BAMS-D-11-001541.

820 Penner, C., 1955: A three-front model for synoptic analyses. *Quart. J. Roy. Meteor. Soc.*, 81
821 (347), 89–91.

822 Pfahl S. and H. Wernli, 2012: Quantifying the relevance of cyclones for precipitation extremes. *J.*
823 *Climate*, 25, 6770-6780, doi:10.1175/JCLI-D-11-00705.1.

824 Posselt, D. J., and J. E. Martin, 2004: The Effect of Latent Heat Release on the Evolution of a
825 Warm Occluded Thermal Structure., *Mon. Wea. Rev.*, **132**, 578-599.

826 Russotto, R.D., J.D.O. Strong, S.J. Camargo, A.H. Sobel, G. Elsaesser, M. Kelley, A.D. Del Genio, Y.
827 Moon, and D. Kim, 2022: Improved representation of tropical cyclones in the NASA GISS-E3
828 GCM. *J. Adv. Model. Earth Syst.*, **14**, no. 1, e2021MS002601, doi:10.1029/2021MS002601.

829 Schultz, D.M., and G. Vaughan, 2011: Occluded fronts and the occlusion process: A fresh look at
830 conventional wisdom. *Bull. Amer. Meteor. Soc.*, 92 (**4**), 443–466.

831 Sinclair V. A. and J. L. Catto, 2023: The relationship between extratropical cyclone intensity and
832 precipitation in idealized current and future climates. *Weather Clim. Dyn.*, 4, 567-589, doi:
833 10.5194/wcd-4-567-2023.

834 Smith, R. N. B., 1990: A scheme for predicting layer clouds and their water content in a general
835 circulation model, *Q. J. Roy. Meteor. Soc.*, 116, 435- 460, doi:10.1002/qj.49711649210.

836 Stephens G. L., D. G. Vane, R. J. Boain, G. G. Mace, K. Sassen, Z. Wang, A. J. Illingworth, E. J.
837 O'Connor, W. B. Rossow, S. L. Durden, S. D. Miller, R. T. Austin, A. Benedetti, C. Mitrescu, and
838 the CloudSat Science Team, 2002: The CloudSat mission and the A-TRAIN: A new dimension
839 to space-based observations of clouds and precipitation. *Bull. Am. Meteorol. Soc.*, **83**, 1771-
840 1790.

841 Stoelinga M. T., J D. Locatelli and P. V. Hobbs, 2002: Warm occlusions, cold occlusions and
842 forward tilting cold fronts. *Bull. Amer. Meteorol. Soc.*, 83, 709-721.

843 Sutcliffe, R., 1947: A contribution to the problem of development. *Quart. J. Roy. Meteor. Soc.*, **73**
844 **(317-318)**, 370–383.

845 Winker D.M., M.A. Vaughan, A.H. Omar, Y. Hu, K.A. Powell, Z. Liu, W.H. Hunt, and S.A. Young,
846 2009: Overview of the CALIPSO Mission and CALIOP Data Processing Algorithms, *J. Atmos.*
847 *Oceanic Technol.*, **26**, 2310-2323.

848 Yettella, V., and J. E. Kay, 2017: How will precipitation change in extratropical cyclones as the
849 planet warms? Insights from a large initial condition climate model ensemble. *Climate Dyn.*,
850 49, 1765–1781, <https://doi.org/10.1007/s00382-016-3410-2>

851 Zhang Z. and B. A. Colle, 2017: Changes in extratropical cyclone precipitation and associated
852 processes during the twenty-first century over Eastern North America and the Western
853 Atlantic using a cyclone-relative approach. *J. Climate*, 30, 8633-8656, doi:10.1175/JCLI-D-16-
854 0906.1.

855

856